Energetic electron precipitation and auroral morphology at the substorm recovery phase

S. Oyama[1], A. Kero[2], C. J. Rodger[3], M. A. Clilverd[4], Y. Miyoshi[1], N. Partamies[5,6], E. Turunen[2], T. Raita[2], P. T. Verronen[7], and S. Saito[1]

1. Institute for Space-Earth Environmental Research, Nagoya University
2. University of Oulu
3. University of Otago
4. British Antarctic Survey
5. The University Centre in Svalbard
6. Birkeland Centre for Space Science, Norway
7. Finnish Meteorological Institute

Abstract

It is well known that auroral patterns at the substorm recovery phase are characterized by diffuse or patch structures with intensity pulsation. According to satellite measurements and simulation studies, the precipitating electrons associated with these aurorae can reach or exceed energies of a few hundred keV through resonant wave-particle interactions in the magnetosphere. However, because of difficulty of simultaneous measurements, the dependency of energetic electron precipitation (EEP) on auroral morphological changes in the mesoscale has not been investigated to date. In order to study this dependency, we have analyzed data from the European Incoherent Scatter (EISCAT) radar, the Kilpisjärvi Atmospheric Imaging Receiver Array (KAIRA) riometer, collocated cameras, ground-based magnetometers, the Van Allen Probe satellites, Polar Operational Environmental Satellites (POES), and the Antarctic-Arctic Radiation-belt (Dynamic) Deposition-VLF Atmospheric Research Konsortium (AARDDVARK). Here we undertake a

detailed examination of two case studies. The selected two events suggest that the highest energy of EEP on those days occurred with auroral patch formation from post-midnight to dawn, coinciding with the substorm onset at local midnight. Measurements of the EISCAT radar showed ionization as low as 65 km altitude, corresponding to EEP with energies of about 500 keV.

1 Introduction

Terrestrial aurora results from the energy release of thermospheric atoms and molecules excited by precipitating charged particles. Most of the precipitating particles are electrons, moving earthward along geomagnetic field lines from the magnetosphere and have energies of 100 eV or higher. Since the auroral-electron energy is several orders of magnitude higher than the typical values of the solar-wind electrons, the acceleration mechanisms to produce such high energies in precipitating electrons has been one of the important subjects in auroral physics. In many previous works, the auroral morphology of substorm activity has been categorized into three stages, that is, growth, expansion and recovery phases, which were introduced by Akasofu [1964] and McPherron [1970]. Previous studies in this field imply that the acceleration and loss mechanisms from the radiation belt tend to coincide with changes in the auroral morphology (as will be discussed in detail later). Therefore it is a natural direction for research activity to undertake comparisons of auroral-morphological evolution with variations in precipitating electron energy at different stages of the substorm.

A representative aurora during the growth and expansion phases consists of a discrete arc, which elongates almost zonally in geomagnetic longitude. A statistical analysis of the auroral morphology has revealed that the longest arc-dominated period is found during the growth phase, and the longest arc waiting times occurs during expansion phase [Partamies et al., 2015]. Equatorward motion is predominant at the growth phase or before the substorm onset, followed by sudden poleward expansions of the aurora, statistically taking place at 65.9 CGM Lat ± 3.5 degrees and 22.9 MLT ± 1.2 hours [Elphinstone et al., 1995]. These aurorae tend to be produced by precipitating electrons which are in the energy range of 1-10s keV. These electrons ionize or excite the neutral particles most efficiently at 100-150 km heights [Rees, 1963; Turunen et al., 2009]. Quasi-static electric fields produce an inverted-V type potential pattern around the geomagnetic field, resulting in auroral electron acceleration over a narrow range of energies [Hallinan and Davis, 1970; Evans, 1974; Mozer et al., 1980; Kletzing et al., 1983]. Discrete arcs are frequently associated with these large quasi-static electric fields due to sharp potential gradients at the edges and relatively constant small electric field inside the arc [Oyama et al., 2009, and references therein]. Broadband aurorae, which are induced by dispersive Alfvén waves, are associated with a wide range of electron precipitation energies, i.e., 10 eV – 10 keV [Ergun et al., 1998; Chaston et al., 2003]. In general, the highest auroral emission intensity at 557.7 nm (atomic oxygen) is found at substorm onset at 10 kR level or higher. According to ground-based magnetic field observations, the growth and the expansion phases take approximately 30-60 minutes and 10-60 minutes, respectively [Wing et al., 2013, and references therein], although there are several results that report different values [Juusola et al., 2011; Partarmies et al., 2015].

Unlike the auroral patterns observed during the growth and expansion phases, the representative features of recovery-phase aurora are diffuse incorporating patches with intensity pulsations. In some cases, particularly in the last half of the recovery phase or dawn-to-noon sector in the magnetic local time (MLT), the auroral structure tends to fragment into patches, drifting toward magnetic east parallel to the direction of ionospheric convection [Nakamura and Oguti, 1987; Shiokawa et al., 2014; Hashimoto et al., 2015]. Diffuse aurora is relatively unstructured, and pulsations in the emission intensity are frequently embedded in the more slowly changing diffuse aurora. Horizontal patterns and temporal variations of the diffuse/pulsating aurora have been studied by many researchers [e.g. Sandahl et al., 1980; Stenbaek-Nielsen, 1980; Yamamoto and Oguti, 1982; Yamamoto, 1988; Nemzek et al., 1995; Nishiyama et al., 2012; Kataoka et al., 2015]. The processes causing the scattering of electrons that lead to the diffuse aurora are believed to be related to resonant wave-particle interactions [e.g. Johnstone et al., 1993; Hikishima et al., 2010; Miyoshi et al., 2010, 2015a; Nishimura et al., 2010; Thorne et al., 2010; Ni et al., 2011; Saito et al., 2012]. The diffuse auroral precipitation electron flux is primarily characterized in energy by a kappa distribution or Maxwellian distribution with a power law tail at the high-energy parts [Kletzing et al., 2003]. Miyoshi et al. [2010] suggested wide energetic electron precipitations (EEP) associated with the diffuse/pulsating aurora, by considering the propagation of whistler mode waves along the magnetic field line. Based on Miyoshi et al. model, a simulation study using GEMSIS-RBW has shown wide energy electron precipitations above a few hundred keV associated with the diffuse/pulsating aurora [Saito et al., 2012]. Recently this prediction was experimentally confirmed using the height-resolved electron density measured with the European Incoherent Scatter (EISCAT) radar and plasma-wave spectra measured with the Van Allen Probe satellite [Miyoshi et al., 2015b]. The EISCAT radar detected ionization in association with pulsating aurora down to height of 68 km, corresponding to EEP with maximum energies of 200 keV (according to the ionization profile by Turunen et al. [2009]). During this event the Van Allen Probe satellite observed rising tone emissions of the lower band chorus (LBC) waves near the equatorial plane. Additional supporting evidence of the >50 keV EEP characteristics was found in the 01-07 MLT sector (at least) through the observations of the Antarctic-Arctic Radiation-belt (Dynamic) Deposition-VLF Atmospheric Research Konsortium (AARDDVARK) [Clilverd et al., 2009]. During this event the Van Allen Probe satellite observed rising tone emissions of the lower band chorus (LBC) waves near the equatorial plane. The computer simulation for the wave-particle interactions [Saito et al., 2012] considering the observed chorus waves well reproduced the observed energy spectrum of precipitating electrons from the EISCAT radar. It is worthwhile to note that the highest energy of EEP is controlled by the latitudinal extension of the propagated chorus waves [Miyoshi et al., 2010, 2015b]. While the Miyoshi et al. [2015b] study focused on a single event without detailed discussion comparing with auroral images, these comprehensive measurements reveal that energy of precipitating electrons can reach hundreds keV in the sector from midnight to dawn, and confirm the theory which suggests this situation should be common. Kurita et al. [2015] showed that MeV electron microbursts of the radiation belts occurred concurrently with the diffuse aurora by analyzing the SAMPEX satellite data and the all-sky imager data at Syowa, Antarctica. The result is also consistent with the model of Miyoshi et al. [2010, 2015b]. It is also important to note that such high-energy precipitation can affect the mesospheric neutral species and, e.g., lead to depletion of ozone by tens of percent during an event (Turunen et al. [2016] and references therein).

The zonally-elongated structure of EEP shown by Miyoshi et al. [2015b] may capture part of the statistical features seen in the global distributions of diffuse auroral precipitation [Newell et al., 2009; Wing et al., 2013]. These statistical studies analyzed DMSP particle data by separating precipitating electron and ion spectra into the four auroral types: mono-energetic, broadband, diffuse, and ion aurorae. The dominant energy flux was found in the diffuse aurora, constituting 84% of the energy flux into the polar ionosphere during periods of low solar wind speed. Diffuse electron energy flux begins to increase after the substorm onset with a broad peak at about 1 hour after onset, confined approximately to the sector spanning 22-09 MLT. The average electron energy gradually increases with MLT from mid-night to noon, and the temporal variation is reproduced by the Auroral Precipitation Model, which shows a broad peak from dawn to noon in the diffuse auroral region at an energy of about 8 keV [Vorobjev et al., 2013]. Increases in the precipitating electron energy can be detected through an associated descent of the peak electron density in the lower ionosphere [Hosokawa and Ogawa, 2015]. That study made a statistical analysis of EISCAT-measured electron density profiles during 21 pulsating-auroral events, and determined that the peak height moves below 100 km after 06 MLT. Oyama et al. [2014] have also shown that the lowest height of the auroral ionization decreases during the recovery phase.

While resonant wave-particle interaction appears to play a key role for the generation of diffuse/pulsating aurora precipitation as discussed above, some statistical studies using measurements at corresponding latitudes from Earth-orbiting satellites or ground-based instruments indicate that the wave activity is not uniformly distributed in MLT [e.g., Koons and Roeder, 1990; Meredith et al., 2003, 2004, 2009; O'Brien et al., 2003; Martinez-Calderon et al., 2015]. Plasmasheet electrons can be scattered into the loss cone through resonant wave-particle interactions by electrostatic cyclotron harmonic (ECH) waves or whistler mode waves [e.g., Thorne et al., 2010]. The ground-based auroral measurements suggest that the recovery-phase aurora is characterized by morphological changes from relatively unstructured patterns to patches, synchronizing with substorm onset at local midnight [Davis, 1978, and references therein]. The horizontal scale of these patches is tens of km or smaller. Because of these very small scales, direct comparisons between plasmasphere/magnetosphere satellite measurements with auroral images taken on the ground have been rarely achieved. In general statistical analysis techniques tend to smooth out any fine structure embedded in the aurora. On the other hand, horizontal patterns of the plasma wave activity cannot be captured from the ground at a horizontal resolution similar as the camera does. Due to these difficulties in measurements, correlations between evolutions of the auroral morphological changes, the wave activity, and EEP have not been well observed synchronically and remain not well understood yet.

In our study we focus on aurora at the substorm recovery phase. From the literature described above, we might be able to predict overall trends in morphology as the recovery-phase aurora is developed from the diffuse type to patches in association with growing amounts of EEP with energies of ~100 keV, if chorus waves propagating along the field line contribute to the pitch angle scattering as suggested by the Miyoshi et al. model. However, our understanding has not yet reached such maturity, particularly regarding the correlation between EEP and morphological changes at the mesoscale. The current study will refine our knowledge in relation to the wave-particle interaction processes in the magnetosphere and how they affect the polar ionosphere. In order to investigate this, we analyze data from the EISCAT radar, the Kilpisjärvi Atmospheric Imaging Receiver Array (KAIRA) riometer [McKay-Bukowski et al., 2015], all-sky cameras, several ground-based magnetometer chains, the MEPED detector onboard the POES satellite, Electric and Magnetic Field Instrument Suite and Integrated Science (EMFISIS) of Van Allen Probe [Kletzing et al., 2013], and AARDDVARK [Clilverd et al., 2009]. More detailed information can be found in Section 2. Two events will be presented in this study: 22-23 January 2014 and 01-02 December 2012. Sections 3.1 and 3.2 will present measurements. The two events will be, at first, separately discussed in Section 4 along with supporting evidences, then compared with the previous results. Section 5 will provide our summary and conclusions.

2. Instruments

In this study, the ionization level due to EEP is evaluated using the EISCAT-measured electron density for event 1 and cosmic noise absorption (CNA) measured with the KAIRA riometer for event 2. The EISCAT radar is located at Tromsø, Norway (Geographic: 69.6°N, 19.2°E; Geomagnetic: 66.7°N, 102.2°E; L = 6.4; LT = UT + 1 hour). During event 1 in 22-23 January 2012, the EISCAT VHF radar was operated, looking geographical zenith, with an alternating code (named as “manda” in the EISCAT community), which consists of a set of 128 different binary-coded pulses with 61 baud codes and baud lengths of 2.4 μs (corresponds to range resolution of 360 m). The receiver signal is damped every about 5 seconds, and to reduce the noise level of the incoherent-scatter spectrum, 60-second time integration has been employed to make figures. The pulse code covers the range from 50 to 207 km. During dark conditions, from 15 UT in 22 January 2012 to 07 UT in 23 January 2012, the collocated all-sky full-color digital camera was also operated under clear sky. The digital camera took an image every minute.

The KAIRA riometer is located at Kilpisjärvi, Finland (Geographic: 69.1°N, 20.8°E; Geomagnetic: 66.1°N, 102.9°E; L = 6.1; LT = UT + 2 hour). For event 2 in 01-02 December 2012, the KAIRA riometer was operated in the two-beam mode; beam 1 looking north-westward (azimuth and elevation angles: 313.95° and 45°, respectively), and beam 2 looking geographical zenith. The available frequencies were from 9.76 to 80.66 MHz; but in this study measurements above 56 MHz are not presented because those measurements tend to be noisy during event 2. An all-sky camera at Kilpisjärvi, which is used in this study, is one of the Magnetometers - Ionospheric Radars - All-sky Cameras Large Experiment (MIRACLE) instrument network in Finland [Sangalli et al., 2011]. Kilpisjärvi all-sky camera imaging standard mode includes 20 images per minute alternating between the three main auroral wavelengths, background wavelengths for each of them, dark frames and non-filtered images. This study uses green line images only (wavelength of 557.7 nm). The standard imaging mode contains 10 of them per minute, with 1.2 second exposure time and an uneven cadence from about three to about ten seconds.

During event 2, NOAA/POES 18 satellite and Van Allen Probes A and B satellites had individual footprints near the area monitored with the ground-based instruments. The measurements of the plasma-wave spectra and the precipitating electrons will be presented in Section 4.2. The AARDDVARK system was in operation during the event 2, and used for estimating the area of precipitating electrons at energy higher than 50 keV. For rough estimation of the substorm-onset region during events 1 and 2, mean ΔH values were derived by using magnetometer chains in Scandinavia (International Monitor for Auroral Geomagnetic Effects; IMAGE), Greenland east and west, Canada (Canadian Array for Realtime Investigations of Magnetic Activity; CARISMA) and Alaska. These values will be referred to as the local AL value in this paper. Note that the KAIRA riometer was not operating for event 1, and the EISCAT radar was not operating for event 2.

3. Observation Results

3.1 Event 1: 22-23 January 2014

Figure 1a shows the electron density measured with the EISCAT VHF radar, looking at the geographical zenith, at 60-110 km for 24 hours from 15 UT in January 22, 2014. Purple dots present cosmic noise absorption (CNA) estimated from the electron density (see Appendix A). The CNA will be used as a supplemental result for discussion of event 2. Low-quality electron density is not shown in the figure. While the background electron density is relatively low, three distinguishable enhancements, marked as T1, T2 and T3, can be seen in the E and D region. There are intervals between the enhancements, which appear to be 4-5 hours in this case. The heights of the peak electron density in each 1 minute time interval are marked by black dots, and they can be seen to decrease in altitude immediately after the commencement of sudden density enhancements. However, the temporal variation of the features seem to be different among the three periods. During the period of T1, the lowest peak height appears at the beginning of the enhancement then gradually recovers upward with decreasing electron density. At 00 UT, almost at the end of T1, the peak height reaches ~110 km. An initial sharp density increase can be seen at 20:40 UT with notably low height of ionization (> ~68 km). During the period of T2, following the sudden drop at 02 UT, the peak height also recovers back to the E region (same as in the case of T1), but only reaching ~105 km, i.e., not relaxing smoothly back to the same altitude as seen at the end of T1. The lowest observed ionization remains at 70-75 km altitude. During the period of T3, the electron density increase is the smallest of the three enhancements. However, the peak height and the lowest height of ionization extend to the lowest levels of all the examples, and with a less obvious recovery from the initial changes during this enhancement. Furthermore electron density enhancements appear intermittent which is a signature not seen during the other two enhancements. While the onset of the T3 enhancement coincides with sunrise (see keogram in panel b), that is by chance because ionization by solar EUV does not cause intermittent enhancements as measured.

To compare with auroral morphology, a keogram is made of a full-color digital camera collocated at the EISCAT radar site (Figure 1b). The keogram shows several intermittent equatorward excursions of the aurora. From 21 to 22 UT, most activities of those excursions are seen at the equatorward side of the zenith. However, just before 22 UT, a sudden brightening occurs with poleward expansion of the arc. This spatiotemporal development is a typical feature of the substorm onset, and the electron-density enhancement observed at T1 is associated with the onset. Following equatorward drift of several arcs during the first half of T1, poleward expansion of bright arcs at ~21:55 UT coincide with obvious enhancements of the electron density and an abrupt decrease of the peak height identified in Figure 1a. During the recovery of the peak height, (approximately from 22:30 to 23:30 UT), diffuse aurora is predominant in the keogram including the zenith or the spot measured with the EISCAT radar. Commencement of the visible auroral activity at T2 is around 01UT, appearing as a faint diffuse pattern in the northern sky. Soon after its appearance, the aurora gradually drifts equatorward, and its equatorward edge approaches the zenith of the site resulting in the E-region electron density increasing at 01-02 UT. Of particular interest to this study is the auroral morphological transformation associated with EEP and ionization enhancements down to the 70-km level. The lowest height of ionization during the diffuse aurora at T1 (from 22:30 to 23:30 UT) was around 80 km or higher. In contrast, during the appearance of diffuse aurora at T2, the lowest height of ionization is lower than the case of T1. While both diffuse aurorae cover the zenith, it is estimated that the precipitation energy is higher at T2 than T1. This feature will be presented in more detail by using next two figures.

Figure 2 is made of the EISCAT and the all-sky camera measurements similar to Figure 1, but zooming into the event from 01 to 03 UT. The height of the peak electron density (indicated by black dots) suddenly drops down from 110 km to 93 km at 02 UT. This change is associated with downward shift of the bottom of ionization height. The electron density continues to increase after the peak height has reached its lowest altitude. The maximum density occurs at 02:10 UT. A faint thin layer seen at 01-02 UT around 95 km in the upper panel is a sporadic E layer, which is out of the scope of this study.

At the beginning of this time period, a faint latitudinally-broad aurora can be seen in the lower panel of Figure 2 that is located ~160 km to the north of the site (corresponding to ~71°N). The arc gradually drifts equatorward until 01:20 UT then stays 110 km north of the site (corresponding to ~70.5°N). The electron-density increase seen above 100 km height after 01:20UT in the upper panel is attributed to auroral precipitation probably at the equatorward edge of this faint aurora. When the electron density increases with a peak-height drop at 02:03 UT, the auroral activity becomes activated above the site, as well as poleward. Periodic increases in the brightness are due to auroral patches marching zonally across the field of view. While such patterns can be identified until 02:45 UT, other patterns characterized by more chaotic boarders appear.

The horizontal pattern can be confirmed in the original all-sky images. Figure 3 presents four representative images from 01:15 to 03:00 UT. The first image (01:15 UT) shows the faint latitudinally-broad aurora near the northern edge of the field-of-view without notable structures in the arc. The aurora visible in the camera image has not yet expanded into the zenith of the site, so the E-region electron density in Figure 1 is still relatively low. The second image taken at 02:00 UT clearly shows that the arc has widened meridionally, and the equator-side edge of the main part of the arc is about to reach the zenith. Since the D-region electron density has already begun to increase, as shown in Figure 2a, it is estimated that some of the auroral activity has intruded into the zenith at that time. At 02:18 UT, one can clearly find evolution of the patch structure on the equatorward side of the faint aurora. In contrast, on the poleward side, the shape of the edge does not change significantly. Compared with the electron density seen in Figure 2a, it is obvious that the equatorward expansion and the patch-structure evolution coincide with EEP development identified with the EISCAT radar. The patches drift eastward evolving into more complicated patterns. At 03:00 UT, the camera field-of-view is almost entirely covered with aurora, although some parts are filled with weak emissions, looking like holes in the image.

3.2 Event 2: 01-02 December 2012

As the EISCAT-measured electron density along with the optical instruments indicates, electrons associated with auroral processes can ionize the atmosphere at both E- and D-region heights. Since a riometer has sensitivity to the ionization at these heights [Rodger et al., 2012], studies of EEP in association with auroral morphological changes can be made using riometer measurements. KAIRA is available for operation in the riometer mode as an extensive use of the Low Frequency Array (LOFAR) antenna in modern wide-band phased-array radio telescope technology. KAIRA is capable of covering two frequency bands; 10-80 MHz and 110-270 MHz. In this study of event 2, at night of 01-02 December 2012, the radio noise absorption measured at 10-50 MHz are presented for finding EEP signatures along with all-sky images collocated at the KAIRA site.

The top two panels of Figure 4 show time-frequency plots of the absorption in two beams from 15-06 UT on 01/02 December 2012: beam 1 directs to the zenith of the Tromsø EISCAT radar site (azimuth and elevation angles: 313.95 and 45 degrees) and beam 2 directs to the zenith of the KAIRA site. The bottom panel shows a meridional keogram made of the all-sky camera. Auroral equatorward drift is clearly seen in the keogram around 18:30-20:30 UT. This is a typical signature of the substorm growth phase. Then the field-of-view is suddenly covered with bright auroral features in association with the substorm onset. The KAIRA riometer CNA also increases at that time at all frequency ranges of the two beams. The magnitude of CNA decreases gradually, particularly at the higher parts of the receiving frequency, exhibiting some sporadic enhancements. From 22 to 00 UT, the sporadic enhancements seem to appear more clearly in measurements in beam 2 (the vertical beam) than those in beam 1 (the northwestward beam). This difference may be attributed to the auroral pattern, which is predominantly seen in the zenith and equatorward, rather than poleward. When the auroral emission intensity enhances before 01 UT, the magnitudes of CNA at both beams also increase. Comparing between CNA and the auroral pattern, we find that CNA magnitude increases with the auroral emission intensity at each measured region.

However, there is an interesting feature in the CNA enhancements after 03 UT. The CNA magnitude is at its largest level in the both beams during this time interval, although notable auroral activity cannot be clearly seen in the keogram in the selected gray scale. Looking at the auroral images more closely, we find an interesting feature as shown in Figure 5. Figure 5 is made of the same data sets as used in Figure 4, except the time interval has been reduced to 02-07 UT in 02 December 2012, and the gray scale of the keogram has been altered to reproduce the features in the data more clearly. A sharply defined arc seen at the bottom part of the keogram is a reflection of the moon. A faint whitish structure seen from 02 to 03 UT in the lower half of the keogram (or the equatorward side from the zenith) is due to thin clouds, although pattern at the upper half is not affected by clouds, and results from auroral activity. The thin clouds have cleared away by 03 UT. In the upper two panels it can be seen that at the frequency range lower than 30 MHz, enhancements of CNA in the beam 1 or the northwestward beam appear earlier than those in the beam 2 or the vertical beam by about 30 minutes. Of particular interest is the morphological change in the auroral image shown in the right panel of Figure 5 during that 30 minutes. Six all-sky images taken from 03:00:02 to 03:19:23 UT are presented on the right hand side of the figure. The first image (at top left, 03:00:02 UT) shows tilted faint aurora in the upper half or the poleward side of the image. No notable features can be found in the auroral pattern. However, in the second image (03:02:23 UT), a zonally-elongated structure begins to develop at the equatorward edge, detaching from the main part of the aurora. At the poleward side of the zonally-elongated structure, several finger-like (or small outgrowth) structures can be identified. In the fourth image (03:10:23 UT), the finger-like structures can be identified more clearly. In the keogram, we can find temporal development of the finger-like structures with the equatorward expansion. One may catch these features in the supplemental movie. Since a plausible northward distance from the zenith (marked as 0 km in the keogram) to the area measured by beam 1 is 63 km under the assumption of 90 km height for generating CNA, it is presumed from the keogram that the beam 1 measures within the aurora feature until about 03:20 UT. However, beam 2 still measures outside of the aurora. With the equatorward expansion of the auroral structure, beam 2 also begins to measure inside of the aurora. It is thus considered that this spatiotemporal evolution is related to the increase of CNA in beam 1 preceding beam 2. The largest CNA for the night (see Figure 4) reasonably suggests that the precipitating electron energy and flux increase occur in association with appearance of auroral patches at 03-05 UT. The majority of the CNA enhancement (e.g. > 1 dB) is attenuated at a faster rate in beam 2 than beam 1 at all frequency ranges. In beam 2 the strong enhancement seems to almost disappear by around 05 UT, when auroral structures move well poleward of the site. Even after 05 UT, some enhancements can be seen in measurements of beam 1 in association with weak but clearly-seen features of auroral emission.

4. Discussion

4.1 Event 1

In the case of event 1, electron-density enhancements take place three times during the observation period. The auroral pattern in the first enhancement (around 22 UT; see Figure 1) shows typical features of substorm onset. Local AL values made of the Scandinavian magnetometers of the IMAGE chain (orange curve in Figure 6) shows a negative peak around 22 UT due to development of the westward ionospheric current at the same time as the first electron-density enhancement. The negative peak around 22 UT can be found in the local AL values made of Greenland-East/West magnetometers. However, the major part of the substorm activity has taken place nearer to Scandinavia than Greenland, according to the magnitude of the signature. There are no notable variations in the Canadian and Alaskan chains. The second and third enhancements of the electron density at Tromsø, Norway begin at 02 and 07 UT, respectively, and the largest negative peaks of the local AL values are found at Greenland East and Canadian chains, respectively. It is considered that these westward shifts of the peak location are primarily due to the Earth’s rotation, which causes an apparent westward shift of the substorm onset region near magnetic midnight. Another important point revealed from Figures 1 and 6 is that electron-density enhancements (caused by EEP) begin with the substorm onset even if the initial substorm injection takes place far from the site of the EEP measurement. The largest magnitude of the local AL value is found at the first substorm activity (i.e. T1) at the Scandinavian sector, then consecutive substorms (i.e. T2 and T3) seem to weaken with time even at the peak location. However, the largest energy of precipitating electrons at Tromsø, Norway is found during the last substorm (i.e. T3). It is thus considered that temporal development of the EEP highly depends on MLT. Furthermore, features of EEP-associated auroral patterns seem to be dependent on MLT. The MLT dependence of EEP will be discussed more in the next paragraph.

Precipitating electron flux was calculated by applying the CARD method [Brekke et al., 1989; Fujii et al., 1995] on individual height profiles of the electron density at T1, T2 and T3 presented in Figure 1a (same as top panel of Figure 7). This method is capable of estimating the flux at 1-170 keV without assuming any mathematical functions (such as Maxwellian) for the spectrum shape. During the first 20-30 minutes of each time interval, mean electron precipitation energies seem to be lower than those in the latter interval. The mean CARD fluxes are calculated separately for the former and latter intervals, respectively, and presented in the lower panels of Figure 7. Two colors are employed to distinguish the results in each time interval. The time interval to make each mean spectrum is written in the figure with same color as the spectrum.

Spectra at T1 and T2 have similar features. The fluxes with characteristic energies below 9 keV exhibit almost no change between the quieter (or former) and the more disturbed (or latter) intervals. However, those fluxes above 10 keV seem to be increased selectively, with larger fluxes in the disturbed (or latter) intervals than the quieter (or former) one. While Maxwellian or other types of functions have been assumed to express the precipitation spectrum in other studies, the spectra during the disturbed intervals are hardly represented by a single traditional function. The spectra in T3 are also characterized by notable increases above 10 keV when comparing between the two intervals. However, fluxes below 10 keV are also slightly increased during the more disturbed interval, which therefore shows a difference in this feature compared with the other two periods.

Figure 8 compares spectra during (a) relatively quieter (or former) intervals and (b) more disturbed (or latter) ones, but all data shown here are same as those in Figure 7. In both cases (a) and (b), T3 has the lowest fluxes in the three at all energies from 1 to 170 keV. The shape of the spectra during T1 and T2 is similar. The most notable difference between T3 and the other two periods is seen in the lower energy part below 40 keV. Fluxes below that energy level seem to be selectively decreased. The EISCAT-measured electron density shown in Figure 1a suggests that the highest precipitating electron energy increases from T1 to T3 according to temporal variations of the lowest height of ionization. However, such behavior cannot be found in Figure 8b because of the upper limitation of the energy range available for the CARD calculation. Since the CARD method cannot derive fluxes above 170 keV (corresponding stopping height is 77 km), we cannot examine ionization below that height.

Figure 9 shows height profiles of the EISCAT-measured electron density averaged for selected time intervals written in the bottom right box. The height profile down to 60 km provides information of the EEP energies exceeding the CARD-derived energy range. Height profile in a geomagnetically quiet condition was estimated by averaging measurements from 15:00 to 17:00 UT in 22 January 2014 (black). There are many gaps seen in Figure 9 below 70 km even after a long-integration time. This can happen at night in the winter months during geomagnetically quiet periods because of rapid recombination at these heights combined with low levels of auroral-particle precipitation. It is thus generally hard to identify the lower threshold of electron density detectable with the EISCAT radar. However, in this case, the base line at 60-70 km can be regarded as 1×10^{9} m^{-3}. Numbers at the right-hand-side of Figure 9b present energies and stopping heights corresponding to individual energies of mono-energetic precipitating electrons are represented by horizontal dashed lines [Turunen et al., 2009]. According to Figure 9a, the electron density associated with the faint latitudinally-broad aurora (see Figure 3) clearly shows positive shifts from the base line above 85 km (light green). A peak at 94 km is due to the sporadic E layer (not due to auroral electrons). After the equatorward expansion and the patch-structure evolution of aurora (see Figure 3), the electron density increased significantly above 73 km but not considerably at 110 km (dark green). The electron density increase suggests that flux of the auroral electrons at energies of 20-200 keV has considerably increased, and that the flux increase coincides with the auroral morphological changes.

The height profile colored in light blue (Figure 9b) is made of measurements at 20:35-20:45 UT. At this time we do not know the physical mechanism to generate such an extremely high EEP around the substorm onset. If we ignore this height profile, the electron densities above 90 km and below 77 km become lower and higher, respectively, at later time intervals. Compared with the stopping heights of mono-energetic electrons, altitudes of 90 and 77 km are equivalent to electrons at energy of about 40 keV and about 200 keV, respectively. Thus from the view point of the precipitation energy, it is revealed that precipitation fluxes at energy lower than about 40 keV and higher than about 200 keV were decreased and increased with time, respectively. The signature of the electron density above 90 km or energy lower than about 40 keV is identical to that seen in the CARD result shown in Figure 8b. However, time evolution of the electron density below 77 km or energy higher than about 200 keV cannot be retrieved in the CARD calculation because it is out of the energy range. Compared with the quiet-time curve (black), the lowest height shifts from 74 km (T1, dark blue) to 72 km (T2, dark green), then 65 km (T3, dark purple). One may find a slightly larger value than the offset (= 1×10^9 m^{-3}) at 63 km height for the time interval of T3 (purple), but that measurement might be a portion of measurement fluctuations because of a data gap at height by one-gate below. Estimated energies from these heights are approximately 200, 300, and 500 keV, respectively. While Miyoshi et al. [2015b] reported ionization at 68 km height from a measurement of the EISCAT radar (corresponding to up to 200 keV), EEP energy of approximately 500 keV is the highest ever inferred from ground-based measurements, for auroral patches. However, uncertainty in the estimated energy may be in order of 100 keV due to combination of several reasons such as ambiguity of the height profile of the ionization rate due to the model-dependency of the neutral density and shortening of the vertical shift of the stopping height below approximately 70 km (see Figure 9). The uncertainty is a disadvantage of this study. The uncertainty can be improved by employing a more mathematical way of the inversion method using, for example, Malkov Chaign Monte Carlo (MCMC) method [Haario et al., 2006], which is planned for a future study.

4.2 Event 2

Sudden enhancements of CNA took place three times during event 2 (from 15 to 07 UT on 01-02 December 2012). As with event 1, local AL indexes were produced using magnetometer data from the four meridian chains as in Figure 10. Around 20:30 UT when the first CNA enhancement occurred at Kilpisjärvi, Finland, there was an obvious sudden development of negative AL value in the Scandinavian and Greenland-East chains. Since the observed magnitude in the Scandinavian chain was about double of that in the Greenland-East chain, the substorm-onset activity probably took place nearer to Scandinavia than the east coast of Greenland. The second CNA enhancement was seen around 01 UT, and again there was development of negative AL values found from Scandinavia to the west coast of Greenland. This indicates an expansion towards the west due to the time shift of the longitude of local midnight. At the third CNA enhancement starting at 03 UT, there is no notable signature at Scandinavia, but negative AL values are persistent in the Greenland-West chain. There are no notable variations in the Canadian and Alaskan chains at this time. While the degree of the westward shift of the peak negative AL location is relatively smaller than that seen during event 1 (see Figure 6), the physical mechanism of the westward shift is considered to be mainly due to the Earth’s rotation as was argued for event 1. The largest magnitude of the local AL values are found in Scandinavia at the first substorm activity in the three substorms. However, the strongest CNA has been measured at the third substorm which began at about 03 UT. The results during event 2 also suggest that temporal development of the EEP depends on MLT. Note, however, that event 2 does not directly suggest that the highest energy of precipitating electron takes place at the third substorm, although the strongest CNA around 04 UT is considerable evidence for the largest electron density at D-region heights. This is because the largest CNA in event 1 does not coincide with the highest energy of precipitating electrons, as shown in Figure 1a. However, the CNA seems to have similar trends with the D-region electron density, which can be understood from Eq. (A1).

In the case of event 2, precipitating electron energy fluxes were observed by the NOAA/POES 18 satellite at 840 km height. There were two passes nearby northern Scandinavia which occurred at (a) 03:11-03:16 UT and (b) 04:53-04:58 UT on 2 December 2012. These passes are shown in Figure 11. It is known that the electron fluxes measured with the POES detector can be contaminated from protons of a few hundred keV energy [Yando et al., 2011]. While event 2 took place in the morning sector, in which electrons tend to be the major particle rather than protons, the possibility of proton contamination to the electron detector has been removed in the analysis. In the former case (a), the satellite flew close by the KAIRA site immediately after commencement of the third CNA enhancement which occurred only in beam 1 (the poleward-looking beam). The NOAA/POES 18 observed at energy of >30 keV (black) and >100 keV (green) electron fluxes shows obvious increases near the site (from 67 to 70°N). A ~30 keV (100 keV) electron would cause peak ionization at ~95 km (~82 km) altitude (see Figure 9). At latitudes lower than 67°N, no notable enhancement of the flux can be identified. Fluxes at >300 keV do not show increases at 55-75°N. The satellite measurements present the equatorward edge of the 30-300keV electron precipitation at 03:11-03:16 UT, showing its location to be near the KAIRA site.

During the second NOAA/POES 18 pass (Figure 11b) from 04:53-04:58 UT, the satellite flew between Norway and Iceland well after commencement of the third CNA enhancement. Figure 5 shows obvious CNA enhancements in the beam 1 (northwestward beam) measurements continue during the satellite pass, although CNA enhancements in the beam 2 (vertical beam) measurements appear to have weakened across most frequencies. The exception are the measurements at the lowest frequencies which remain at a comparatively high level. In this case the >30 keV and >100 keV precipitating fluxes enhance at wider range of latitude than seen during the first pass. The latitudinal expansion is equivalent to an equatorward expansion of the aurora as revealed in the keogram (see Figure 5). However, again precipitating fluxes at energies larger than 300 keV do not show a detectable enhancement. These satellite measurements suggest that at these times the dominant precipitating electrons are those with energies of 30-300 keV level which ionizes the mesosphere and the lower thermosphere (> 71 km height; see Figure 9), resulting in the observed CNA enhancements.

Further supporting evidences come both from the AARDDVARK network observations and the measurements made onboard the Van Allen Probe A/B satellites. These are presented in Figure 12. The two orange lines in panel (a) present reasonable edges of the precipitation estimated by the AARDDVARK observations, through analysis of the response in this region. The AARDDVARK network in this region consists of 8 receivers each detecting ~10 subionospheric transmitter signals from a variety of locations. In this way a network of great circle subionospheric propagation paths crosses the region with some paths showing amplitude and phase perturbation responses to the EEP, and some not [e.g., see Figure 2 in Clilverd et al., 2009]. The observations suggest the presence of an extended region of precipitation. Note however the eastern edge of the EEP region, shown in Figure 12a, in Scandinavia is slightly arbitrary because there are no available receivers over Russia. There is evidence of precipitation at locations further north, although this is mainly provided by examination of the paths from the Iceland VLF transmitter, which generally shows large amounts of variability on many of the paths. However, the area between the orange lines is a reasonable description of where electron precipitation at energies of >50 keV occurs within the region (the lower energy limit being determined by the ambient nighttime D-region [Rodger et al., 2012]). Note that horizontal resolution of the AARDDVARK network may not be sufficiently high enough to reproduce the spatial gradient of EEP. Figure 12a shows the footprints of the Van Allen Probe A (red) and B (blue) satellites from 03 to 06 UT in 02 December 2012. These are located at Scandinavia and west of Iceland, respectively. The footprints stay inside of the precipitation area determined by the AARDDVARK observations during this event from 03-04 UT. The Van Allen Probe A footprint (red) is located at more northward than the Van Allen Probe B one (blue) during the event time. According to WFR spectra measured with EMFISIS, evidence of lower band chorus (LBC) is clearly seen in the Van Allen Probe A EMFISIS data (at least after 02:40 UT). This is earlier than when chorus emissions are seen on Van Allen Probe B, which begins at 03 UT. The LBC mainly contribute to the precipitations above a few keV electrons, while the upper-band chorus (UBC) cause precipitations less than a few keV [e.g., Thorne et al., 2010, Miyoshi et al., 2015a]. As has been suggested by the Miyoshi et al. model, above a tens keV electron precipitations are expected if the LBC propagates to the higher-latitudes. It has previously been recognized that lower-band chorus can cause scattering loss of higher energy electrons (10-50 keV level) more effectively than the scattering by upper-band chorus (1-10 keV level) [Kennel and Petschek, 1966; Kennel and Thorne, 1967; Li et al., 2010]. Figure 12 suggests that precipitating electrons at an energy of about 100 keV driven by whistler mode chorus should first appear in relatively northward locations and then expand equatorward. This pattern is consistent with the KAIRA results.

4.3 Comprehensive discussion

Two events were analyzed in this study; event 1 with the EISCAT radar and event 2 with the KAIRA riometer. Both measurements were supported by other ground-based and satellite observations. While the results from these observations are summarized in this section, it should be noted that we need further studies in the future with more events to assess the validity of the summary by analyzing more examples, in particular to better understand the energy evolution of the precipitating electrons with time.

During the two events, the substorm onsets have occurred three times a day with interval of 3-4 hours. While the geomagnetic activity was moderately high, these multiple onsets are not unusual [Partamies et al., 2013]. We thus presume that similar ionospheric responses can occur in other cases. Every time the substorm activity started between Scandinavian and Alaskan longitudes, the ionospheric electron density increased in the Scandinavian region due to the electron precipitation. The highest energy of the precipitating electrons for each substorm activity tended to increase with MLT, in particular, maximizing in the late morning or pre-noon time. The EISCAT-measured electron density showed ionization at about 65 km, corresponding to about 500 keV energy of the mono-energetic electron precipitation. Precipitating mono-energetic electrons at energies higher than about 200 keV had the tendency of increasing in flux with MLT. In contrast, those at energies lower than about 40 keV had the opposite tendency. Comparison with the all-sky auroral images revealed that the EEP start coincided with the development of finger-like (or small outgrowth) structures at the equatorward edge of the northern diffuse aurora. The AARDDVARK receivers and the Van Allen Probe satellites suggest the presence of zonally extended regions of EEP associated with lower-band chorus wave for the times when the KAIRA riometer detected obvious CNA enhancements.

Changes in auroral morphology at the substorm recovery phase are characterized by repetition for every substorm as mentioned in Section 1. The diffuse aurora gradually, but on some occasions suddenly transforms to patch structures. In cases of this study, this occurs at the equatorward side of the diffuse aurora. While the morphological changes appear predominantly from post-midnight to dawn, the chorus-wave activity also tends to be high in the same MLT region. It is well known that chorus waves play a key role in EEP generation in the diffuse/pulsating aurorae. Combining with the observation results in our study, simultaneous growth of the auroral patch and EEP suggests that the chorus-wave activity also relates to the generation mechanism of the auroral patch. Formation of the auroral patch was recently studied by Shiokawa et al. [2014] and Hashimoto et al. [2015]. A concept of auroral fragmentation was proposed in their study by introducing the hypothesis that magnetospheric instabilities induced by the force balance between the radial gradients of plasma pressure and the earthward magnetic-tension force are mapped down to the polar ionosphere. In this case the gradient of the magnetospheric-plasma pressure represents the horizontal pattern of the plasma density. An increase in the plasma density would induce resonance of waves with the electron population, containing a source of free energy for the wave generation [Li et al., 2011]. Integration of these results suggests that EEP, patch formation and chorus wave are manifestations resulting from the same phenomenon in the magnetosphere and ionosphere.

5. Summary and conclusions

In this study we have reported on EEP measured during two event periods. In both cases precipitation during the substorm recovery phase were compared with changes in the observed auroral morphology. In event 1 the EEP was identified from measurements with the EISCAT radar, for 24 hours from 15 UT in 22 January 2014. In event 2 the EEP observations were provided with the KAIRA riometer, for 16 hours from 15 UT in 01 December 2012. All-sky cameras collocated at the individual measurement sites were used for monitoring the auroral morphology. Of particular interest was EEP development that coincided with generation of the auroral patches. The lowest height of ionization found in this study was 65 km, corresponding to stopping height of precipitating mono-energetic electron with energy of about 500 keV, although the estimated uncertainty might be of order of 100 keV. The precipitation energy tended to increase with MLT even though the geomagnetic activity level tended to decrease with MLT. Measurements from the AARDDVARK system and the Van Allen Probes A/B satellites suggested that EEP took place across a zonally extended area. Lower-band chorus waves were detected with the Van Allen Probe satellites during EEP, which is understandable as chorus wave-particle interactions with the chorus will cause scattering leading to the EEP. These comprehensive measurements intuitively suggest that the highest energy of auroral electrons appear inside of the auroral patch, and that generation of the auroral patch, EEP and lower-band chorus wave can be understood as the main elements of a causal chain of diffuse aurora dynamics.

Acknowledgments

We are indebted to the director and staff of EISCAT for operating the facility and supplying the data. EISCAT is an international association supported by research organizations in China (CRIPR), Finland (SA), Japan (ISEE and NIPR), Norway (NFR), Sweden (VR), and the United Kingdom (STFC). We thank the institutes who maintain the IMAGE magnetometer array. KAIRA was funded by the University of Oulu and the FP7 European Regional Development Fund and is operated by Sodankylä Geophysical Observatory. We thank the institutes who maintain the IMAGE magnetometer array and the people maintaining, operating and calibrating the MIRACLE Kilpisjärvi camera. The AARDDVARK observations were obtained through funding support from the European Union Seventh Framework Programme [FP7/2007-2013] under PLASMON grant agreement n°263218. This research has been supported by a Grant-in-Aid for Scientific Research (15H05747, 15H05815, 16H06286, 16K05569, 16H02230) and Special Funds for Education and Research (Energy Transport Processes in Geospace) from MEXT, Japan. P.T.V. was funded by the Academy of Finland through the project #276926 (SECTIC: Sun-Earth Connection Through Ion Chemistry). A.K.'s work was funded by European Regional

Development Fund (Regional Council of Lapland, decision number A70179). N.P was funded by Research Council of Norway/CoE under contract 223252/F50.

Appendix A: Estimation of the cosmic noise absorption from the EISCAT-measured electron density

The cosmic noise absorption (CNA) is usually measured with the riometer, but can be calculated from Eq. A1.

$$\mathrm{CNA} = 4.65 \times 10^{-5} \int_{65km}^{120km} \frac{N_e(h)\nu_{en}(h)}{\omega^2 + \nu_{en}^2(h)} dh \qquad \text{(A1)}$$

where N_e is the height-resolved electron density, and EISCAT measurements were used to make Figure 1a. ν_{en} is the electron-neutral collision frequency, and ω is angular frequency of the radio wave (in radian) to be applied to the riometer measurement. We assumed 30 MHz to make Figure 1a. For the ν_{en} calculation, NRLMSISE-00 model [Picone et al., 2002] was used in Eq. A2 [Dalgarno et al., 1967].

$$\nu_{en} = 1.7 \times 10^{-11}[N_2]T + 3.8 \times 10^{-10}[O_2]T^{1/2} + 1.4 \times 10^{-10}[O]T, \qquad \text{(A2)}$$

where T is the temperature, and $[N_2]$, $[O_2]$, and [O] are density (cm^{-3}) of each molecular and atom. Precisely speaking, CNA due to precipitating auroral electrons should have been calculated using the electron density after removing the background level. However, we treated the background level as unimportant for the CNA estimation in this study because of low background ionization in polar winter.

References

Akasofu, S.-I. (1964), The development of the auroral substorm, Planet. Space Sci., 12, 273–282.

Brekke, A., C. Hall, and T. L. Hansen (1989), Auroral ionospheric conductances during disturbed conditions, Ann. Geophys., 7, 269–280.

Chaston, C. C., J. W. Bonnell, C. W. Carlson, J. P. McFadden, R. E. Ergun, and R. J. Strangeway (2003), Properties of small-scale Alfve ´n waves and accelerated electrons from FAST, J. Geophys. Res., 108(A4), 8003, doi:10.1029/2002JA009420.

Clilverd, M. A., C. J. Rodger, N. R. Thomson, J. B. Brundell, T. Ulich, J. Lichtenberger, N. Cobbett, A. B. Collier, F. W. Menk, A. Seppälä, P. T. Verronen, and E. Turunen (2009), Remote sensing space weather events: the AARDDVARK network, Space Weather, 7, S04001, doi: doi:10.1029/2008SW000412.

Dalgrno et al. (1967), The diurnal variation of ionospheric temperatures, Planet. Space Sci., 15, 331-345.

Davis, T. N. (1978), Observed characteristics of auroral forms, Space Sci. Rev., 22(1), 77-113.

Elphinstone, R. D., et al. (1995), Observations in the vicinity of substorm onset: Implications for the substorm process, J. Geophys. Res., 100(A5), 7937–7969, doi:10.1029/94JA02938.

Ergun, R. E., et al. (1998), FAST satellite observations of electric field structures in the auroral zone, Geophys. Res. Lett., 25, 2025, doi:10.1029/98GL00635.

Evans, D. S. (1974), Precipitating electron fluxes formed by a magnetic field aligned potential difference, J. Geophys. Res., 79, 2853, doi:10.1029/JA079i019p02853.

Fujii, R., S. Nozawa, M. Sato, N. Matuura, T. Ono, A. Brekke, C. Hall, and T. L. Hansen (1995), Comparison between electron spectra calculated from EISCAT electron density profiles and those observed by the DMSP satellites, J. Geomagn. Geoelectr., 47, 771–782.

Haario, H., Laine, M., Mira, A. et al. (2006), DRAM: Efficient adaptive MCMC, Stat Comput, 16: 339. doi:10.1007/s11222-006-9438-0.

Hallinan, T. J., and T. N. Davis (1970), Small-scale auroral arc distortions, Planet. Space Sci., 18, 1735, doi:10.1016/0032-0633(70)90007-3.

Hashimoto, A., K. Shiokawa, Y. Otsuka, S.-i. Oyama, S. Nozawa, T. Hori, M. Lester, and M. G. Johnsen (2015), Statistical study of auroral fragmentation into patches, J. Geophys. Res. Space Physics, 120, 6207–6217, doi:10.1002/2015JA021000.

Hikishima, M., Y. Omura, and D. Summers (2010), Microburst precipitation of energetic electrons associated with chorus wave generation, Geophys. Res. Lett., 37, L07103, doi:10.1029/2010GL042678.

Hosokawa, K., and Y. Ogawa (2015), Ionospheric variation during pulsating aurora, J. Geophys. Res. Space Physics, 120, 5943–5957, doi:10.1002/2015JA021401.

Johnstone, A. D., D. M. Walton, R. Liu, and D. A. Hardy (1993), Pitch angle diffusion of low-energy electrons by whistler mode waves, J. Geophys. Res., 98(A4), 5959–5967, doi:10.1029/92JA02376.

Juusola, L., N. Østgaard, E. Tanskanen, N. Partamies, and K. Snekvik (2011), Earthward plasma sheet flows during substorm phases, J. Geophys. Res., 116, A10228, doi:10.1029/2011JA016852.

Kataoka, R., Y. Fukuda, Y. Miyoshi, H. Miyahara, S. Itoya, Y. Ebihara, D. Hampton, H. Dahlgren, D. Whiter, and N. Ivchenko (2015), Compound auroral micromorphology: ground-based high-speed imaging, Earth, Planets and Space, 67:23, doi: 10.1186/s40623-015-0190-6.

Kennel, C. F., and H. E. Petschek (1966), Limit on stably trapped particle fluxes, J. Geophys. Res., 71(1), 1–28, doi:10.1029/JZ071i001p00001.

Kennel, C. F., and R. M. Thorne (1967), Unstable growth of unducted whistlers propagating at an angle to the geomagnetic field, J. Geophys. Res., 72(3), 871–878, doi:10.1029/JZ072i003p00871.

Kletzing, C., C. Cattell, F. S. Mozer, S.-I. Akasofu, and K. Makita (1983), Evidence for electrostatic shocks as the source of discrete auroral arcs, J. Geophys. Res., 88, 4105, doi:10.1029/JA088iA05p04105.

Kletzing, C. A., J. D. Scudder, E. E. Dors, and C. Curto (2003), The auroral source region: Plasma properties of the high altitude plasma sheet, J. Geophys. Res., 108(A10), 1360, doi:10.1029/2002JA009678.

Kletzing, C. A., et al. (2013), The electric and magnetic field instrument suite and integrated studies (EMFISIS) on RBSP, Space Sci. Rev., 179, 127–181.

Koons, H. C., and J. L. Roeder (1990), A survey of equatorial magnetospheric wave activity between 5 and 8 R_E, Planet. Space. Sci., 38(10), 1335-1341.

Kurita, S., A. Kadokura, Y. Miyoshi, A. Morioka, Y. Sato, and H. Misawa (2015), Relativistic electron precipitations in association with diffuse aurora: Conjugate observation of SAMPEX and the all sky TV camera at Syowa Station, Geophys. Res. Lett., 42, 4702-4208, doi:10.1002/2015GL064564.

Li, W., et al. (2010), THEMIS analysis of observed equatorial electron distributions responsible for the chorus excitation, J. Geophys. Res., 115, A00F11, doi:10.1029/2009JA014845.

Li, W., J. Bortnik, R. M. Thorne, Y. Nishimura, V. Angelopoulos, and L. Chen (2011), Modulation of whistler mode chorus waves: 2. Role of density variations, J. Geophys. Res., 116, A06206, doi:10.1029/2010JA016313.

Martinez-Calderon, C., K. Shiokawa, Y. Miyoshi, M. Ozaki, I. Schofield, and M. Connors (2015), Statistical study of ELF/VLF emissions at subauroral latitudes in Athabasca, Canada, J. Geophys. Res. Space Physics, 120, 8455–8469, doi:10.1002/2015JA021347.

McKay-Bukowski, D., et al. (2015), KAIRA: The Kilpisjärvi Atmospheric Imaging Receiver Array; System Overview and First Results, Geoscience and Remote Sensing, IEEE Transactions on, 53(3), 1440-1451, doi:10.1109/TGRS.2014.2342252.

McPherron, R. L. (1970), Growth phase of magnetospheric substorms, J. Geophys. Res., 75, 5592–5599, doi:10.1029/JA075i028p05592.

Meredith, N. P., R. M. Thorne, R. B. Horne, D. Summers, B. J. Fraser, and R. R. Anderson (2003), Statistical analysis of relativistic electron energies for cyclotron resonance with EMIC waves observed on CRRES, J. Geophys. Res., 108, 1250, doi:10.1029/2002JA009700, A6.

Meredith, N. P., R. B. Horne, R. M. Thorne, D. Summers, and R. R. Anderson (2004), Substorm dependence of plasmaspheric hiss, J. Geophys. Res., 109, A06209, doi:10.1029/2004JA010387.

Meredith, N. P., R. B. Horne, R. M. Thorne, and R. R. Anderson (2009), Survey of upper band chorus and ECH waves: Implications for the diffuse aurora, J. Geophys. Res., 114, A07218, doi:10.1029/2009JA014230.

Miyoshi, Y., Y. Katoh, T. Nishiyama, T. Sakanoi, K. Asamura, and M. Hirahara (2010), Time of flight analysis of pulsating aurora electrons, considering wave-particle interactions with propagating whistler mode waves, J. Geophys. Res., 115, A10312, doi:10.1029/2009JA015127.

Miyoshi, Y. et al. (2015a), Relation between energy spectra of pulsating aurora electrons and frequency spectra of whistler-mode chorus waves, J. Geophys. Res., 120, 7728-7736, doi:10.1002/2015JA021562.

Miyoshi, Y., et al. (2015b), Energetic electron precipitation associated with pulsating aurora: EISCAT and Van Allen Probe observations, J. Geophys. Res. Space Physics, 120, doi:10.1002/2014JA020690.

Mozer, F. S., C. A. Cattell, M. K. Hudson, R. L. Lysak, M. Temerin, and R. B. Torbert (1980), Satellite measurements and theories of low altitude auroral particle acceleration, Space Sci. Rev., 27, 155, doi:10.1007/BF00212238.

Nakamura, R., and T. Oguti (1987), Drifts of auroral structures and magnetospheric electric fields, J. Geophys. Res., 92, 11,241–11,247, doi:10.1029/JA092iA10p11241.

Nemzek, R. J., Nakamura, R., Baker, D. N., Belian, R. D., McComas, D. J., Thomsen, M. F., and Yamamoto, T. (1995), The relationship between pulsating auroras observed from the ground and energetic electrons and plasma density measured at geosynchronous orbit, J. Geophys. Res., 100(A12), 23935–23944.

Newell, P. T., T. Sotirelis, and S. Wing (2009), Diffuse, monoenergetic, and broadband aurora: The global precipitation budget, J. Geophys. Res., 114, A09207, doi:10.1029/2009JA014326.

Ni, B., R. M. Thorne, N. P. Meredith, Y. Y. Shprits, and R. B. Horne (2011), Diffuse auroral scattering by whistler mode chorus waves: Dependence on wave normal angle distribution, J. Geophys. Res., 116, A10207, doi:10.1029/2011JA016517.

Nishimura, Y., et al. (2010), Identifying the driver of pulsating auroras, Science, 330, 81.

Nishiyama, T., et al. (2012), Fine scale structures of pulsating auroras in the early recovery phase of substorm using ground-based EMCCD camera, J. Geophys. Res., 117, A10229, doi:10.1029/2012JA017921.

O'Brien, T. P., et al. (2003), Energization of relativistic electrons in the presence of ULF power and MeV microbursts: Evidence for dual ULF and VLF acceleration, J. Geophys. Res., 108, 1329, doi:10.1029/2002JA009784, A8.

Oyama, S., et al. (2009), Spatial evolution of frictional heating and the predicted thermospheric wind effects in the vicinity of an auroral arc measured with the Sondrestrom incoherent-scatter radar and the Reimei satellite, J. Geophys. Res., 114, A07311, doi:10.1029/2009JA014091.

Oyama, S., Y. Miyoshi, K. Shiokawa, J. Kurihara, T. T. Tsuda, and B. J. Watkins (2014), Height-dependent ionospheric variations in the vicinity of nightside poleward expanding aurora after substorm onset, J. Geophys. Res. Space Physics, 119, 4146–4156, doi:10.1002/2013JA019704.

Partamies, N., L. Juusola, E. Tanskanen and K. Kauristie (2013), Statistical properties of substorms during different storm phases, Ann. Geophys., 31, 349–358, doi: 10.5194/angeo-31-349-2013.

Partamies, N., L. Juusola, D. Whiter, and K. Kauristie (2015), Substorm evolution of auroral structures, J. Geophys. Res. Space Physics, 120, 5958–5972, doi:10.1002/2015JA021217.

Picone, J. M., A. E. Hedin, D. P. Drob, and A. C. Aikin (2002), NRLMSISE-00 empirical model of the atmosphere: Statistical comparisons and scientific issues, J. Geophys. Res., 107(A12), 1468, doi:10.1029/2002JA009430.

Rees, M. H. (1963), Auroral ionization and excitation by incident energetic electrons, Planet Space Sci., 11, 1209-1218.

Rodger, C. J., M. A. Clilverd, A. J. Kavanagh, C. E. J. Watt, P. T. Verronen, and T. Raita (2012), Contrasting the responses of three different groundbased instruments to energetic electron precipitation, Radio Sci., 47, RS2021, doi:10.1029/2011RS004971.

Saito, S., Y. Miyoshi, and K. Seki (2012), Relativistic electron microbursts associated with whistler chorus rising tone elements: GEMSIS-RBW simulation, J. Geophys. Res., 117, A10206, doi:10.1029/2012JA018020.

Sandahl, I., Eliasson, L., and Jundin, R. (1980), Rocket observations of precpitating electrons over a pulsating aurora, Geophys. Res. Lett., 7(5), 309–312.

Sangalli, L., N. Partamies, M. Syrjäsuo, C.-F. Enell, K. Kauristie, and S. Mäkinen (2011), Performance study of the new EMCCD-based all-sky cameras for auroral imaging, International Journal of Remote Sensing, 32, 2987–3003, dpi:10.1080/01431161.2010.541505.

Shiokawa, K., et al. (2014), Auroral fragmentation into patches, J. Geophys. Res. Space Physics, 119, 8249–8261, doi:10.1002/2014JA020050.

Stenbaek-Nielsen, H. C. (1980), Pulsating aurora: The importance of the ionosphere, Geophys. Res. Lett., 7(5), 353–356.

Thorne, R. M., B. Ni, X. Tao, R. B. Horne, and N. P. Meredith (2010), Scattering by chorus waves as the dominant cause of diffuse aurora precipitation, Nature, 467(7318), 943–946.

Turunen, E., P. T. Verronen, A. Sepp¨al¨a, C. J. Rodger, M. A. Clilverd, J. Tamminen, C.-F. Enell, and T. Ulich (2009), Impact of different precipitation energies on NOx generation during geomagnetic storms, J. Atmos. Sol.-Terr. Phys., 71, 1176–1189, doi:436 10.1016/j.jastp.2008.07.005.

Turunen, E., A. Kero, P. Verronen, Y. Miyoshi, S. Oyama, and S. Saito (2016), Mesospheric ozone destruction by high-energy electron precipitation associated with pulsating aurora, J. Geophys. Res. Atmos., 2016JD025015, accepted.

Vorobjev, V. G., O. I. Yagodkina, and Yu. V. Katkalov (2013), Auroral precipitation model and its applications to ionospheric and magnetospheric studies, J. Atmos. Solar-Terr. Phys., 102, 157-171, doi:10.1016/j.jastp.2013.05.007.

Wing, S., M. Gkioulidou, J. R. Johnson, P. T. Newell, and C.-P. Wang (2013), Auroral particle precipitation characterized by the substorm cycle, J. Geophys. Res. Space Physics, 118, 1022–1039, doi:10.1002/jgra.50160.

Yamamoto, T. and Oguti, T. (1982), Recurrent fast motions of pulsating auroral patches 1. A case study on optical and quantitative characteristics during a slightly active period, J. Geophys. Res., 87(A9), 7603–7614.

Yamamoto, T. (1988), On the temporal fluctuations of pulsating auroral luminosity, J. Geophys. Res., 93(A2), 897–911.

Yando, K., R. M. Millan, J. C. Green, and D. S. Evans (2011), A Monte Carlo simulation of the NOAA POES Medium Energy Proton and Electron Detector instrument, J. Geophys. Res., 116, A10231, doi:10.1029/2011JA016671.

Figure 1.

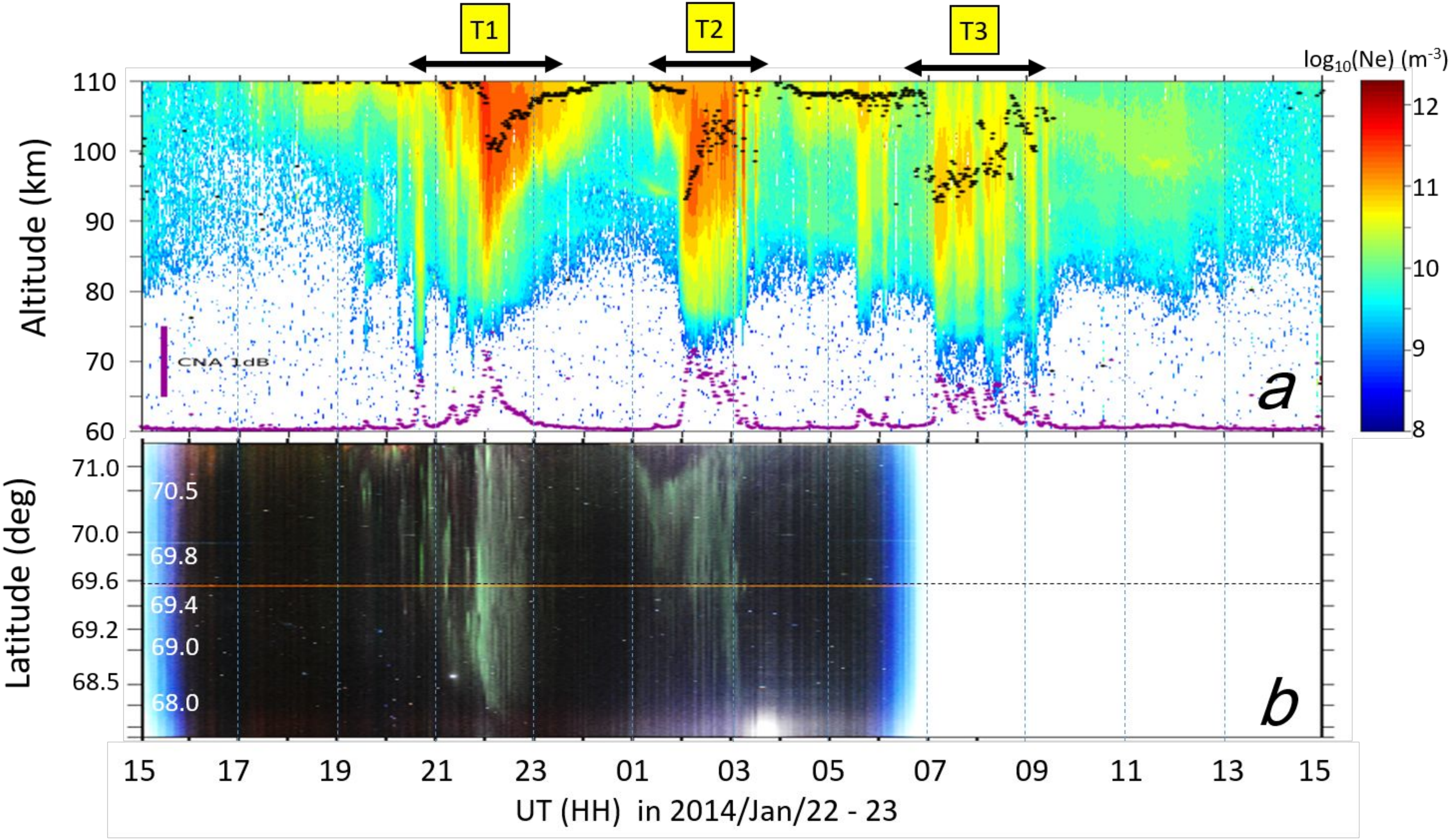

Figure 1: (a) Electron density measured with the EISCAT VHF radar at 60-110 km height for 24 hours from 15 UT in 22 January 2014. Black dots present a height where the electron density peaks during each integration period (1 minute). Purple dots present CNA (dB) estimated from the EISCAT-measured electron density (a horizontal line of 60 km height corresponds to 0 dB for the CNA. Scale of 1 dB is marked in the figure). (b) keogram made of an all-sky camera images taken from 15 to 07 UT in 22-23 December 2014 at the Tromsø EISCAT radar site, which is marked by a horizontal red line. Three time intervals focused in this study are highlighted by yellow boxes and arrows at the top of panel (a).

Figure 2.

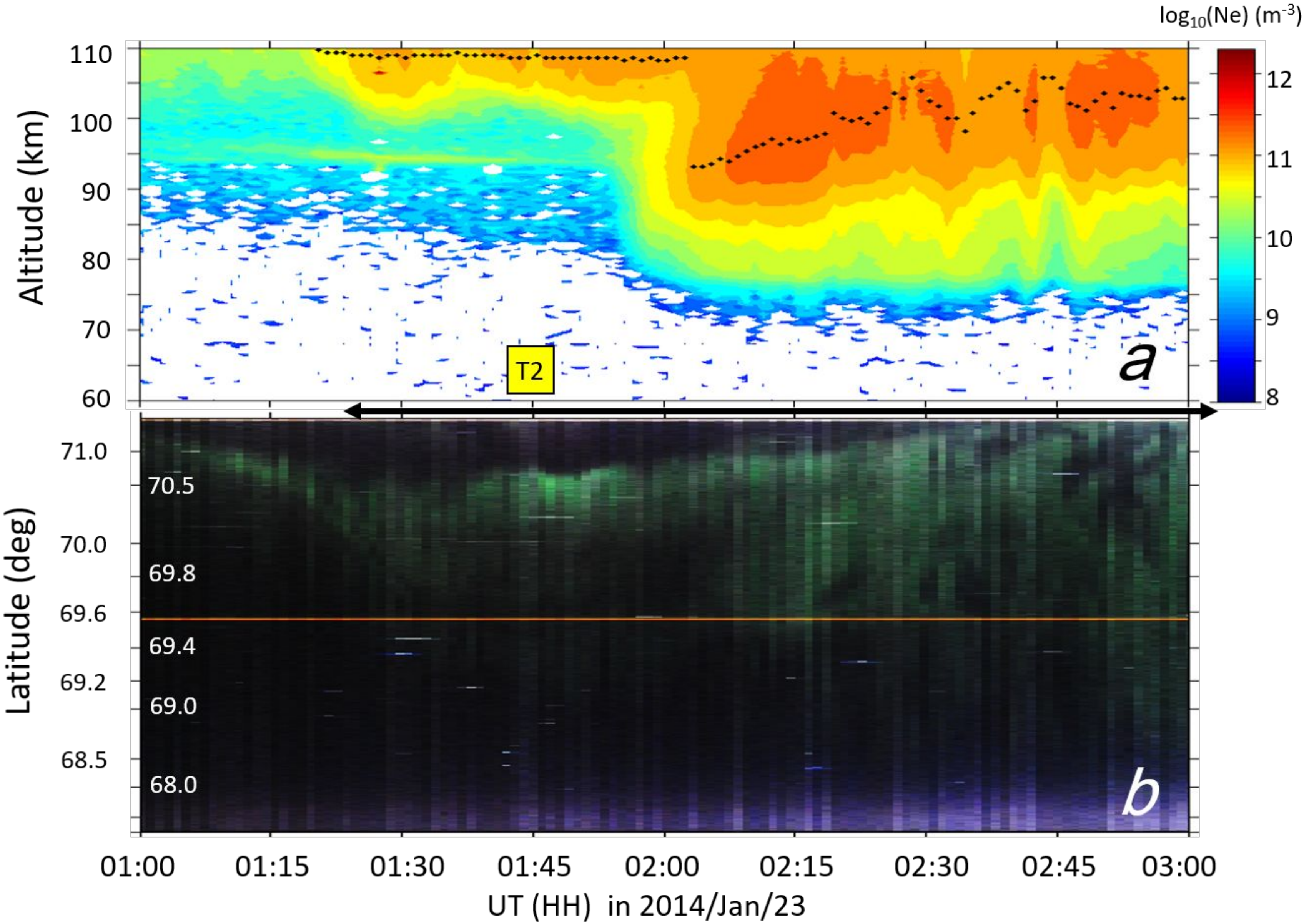

Figure 2: Electron density and keogram, which are the same format as Figure 1, but from 01 to 03 UT in 23 January 2014.

Figure 3.

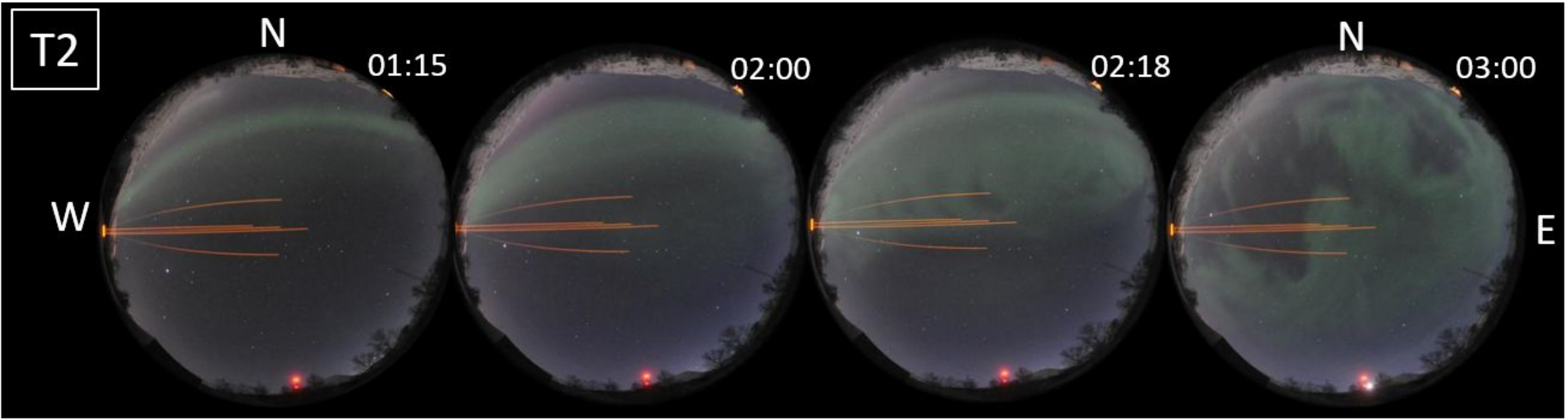

Figure 3: Four all-sky images taken at the Tromsø all-sky camera at 01:15, 02:00, 02:18, and 03:00 UT (from left to right) in 23 January 2014. Top and right of each image are north and east, respectively. Five orange beams of a sodium LIDAR and a red obstacle light are contaminated into photos.

Figure 4.

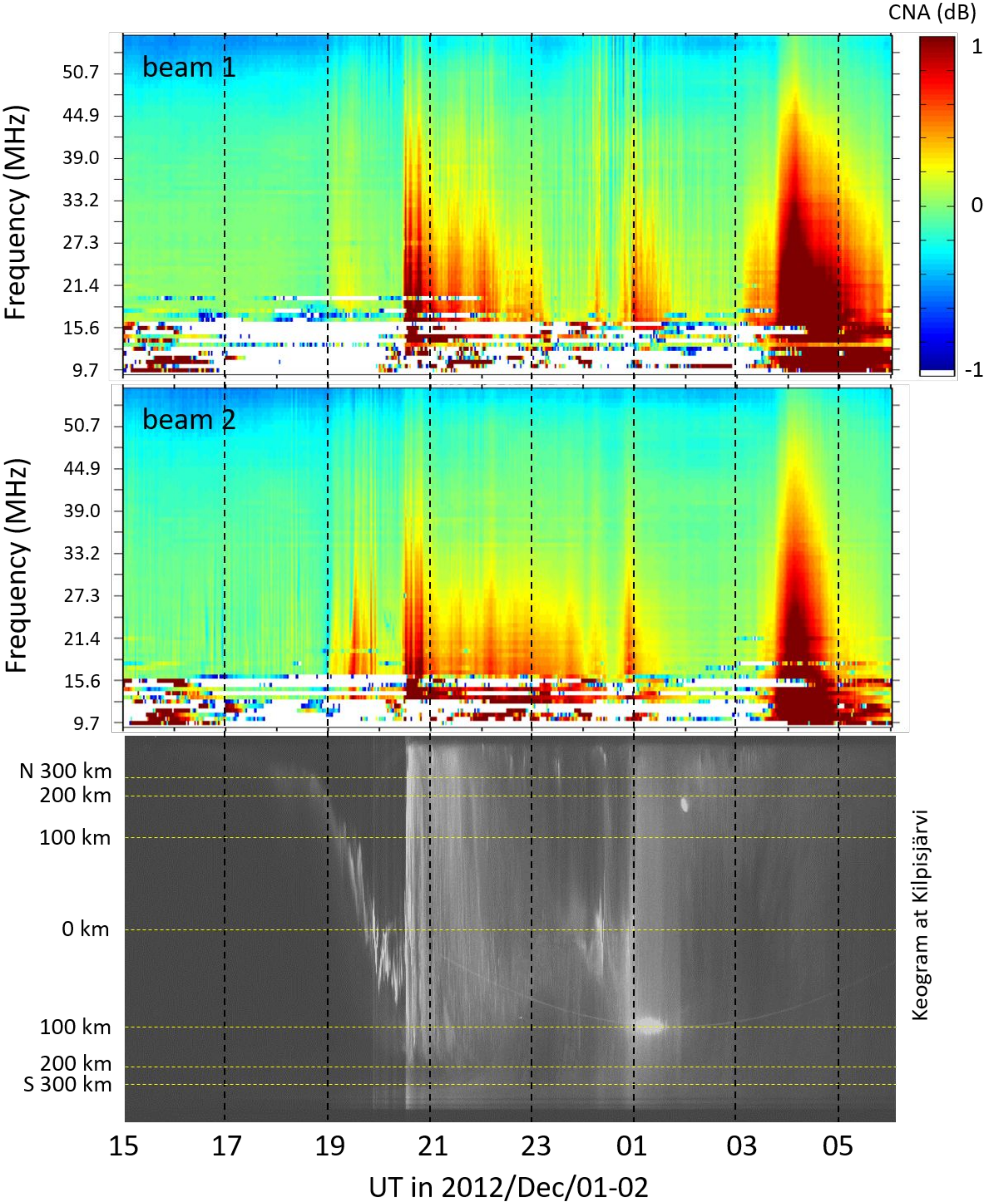

Figure 4: Top two panels: CNA measured with the KAIRA beam 1 (northwestward) and beam 2 (vertical) at multiple frequencies from 15 to 07 UT in 01-02 December 2012. Magnitude of CNA is presented in dB (its color scale is right-hand-side). Bottom panel: meridional keogram made of all-sky images taken with a camera collocated at KAIRA in Kilpisjärvi, Finland. A white dot around 01 UT (at 100km distance southward) and associated stable faint arc are due to dome reflection of the lunar light.

Figure 5.

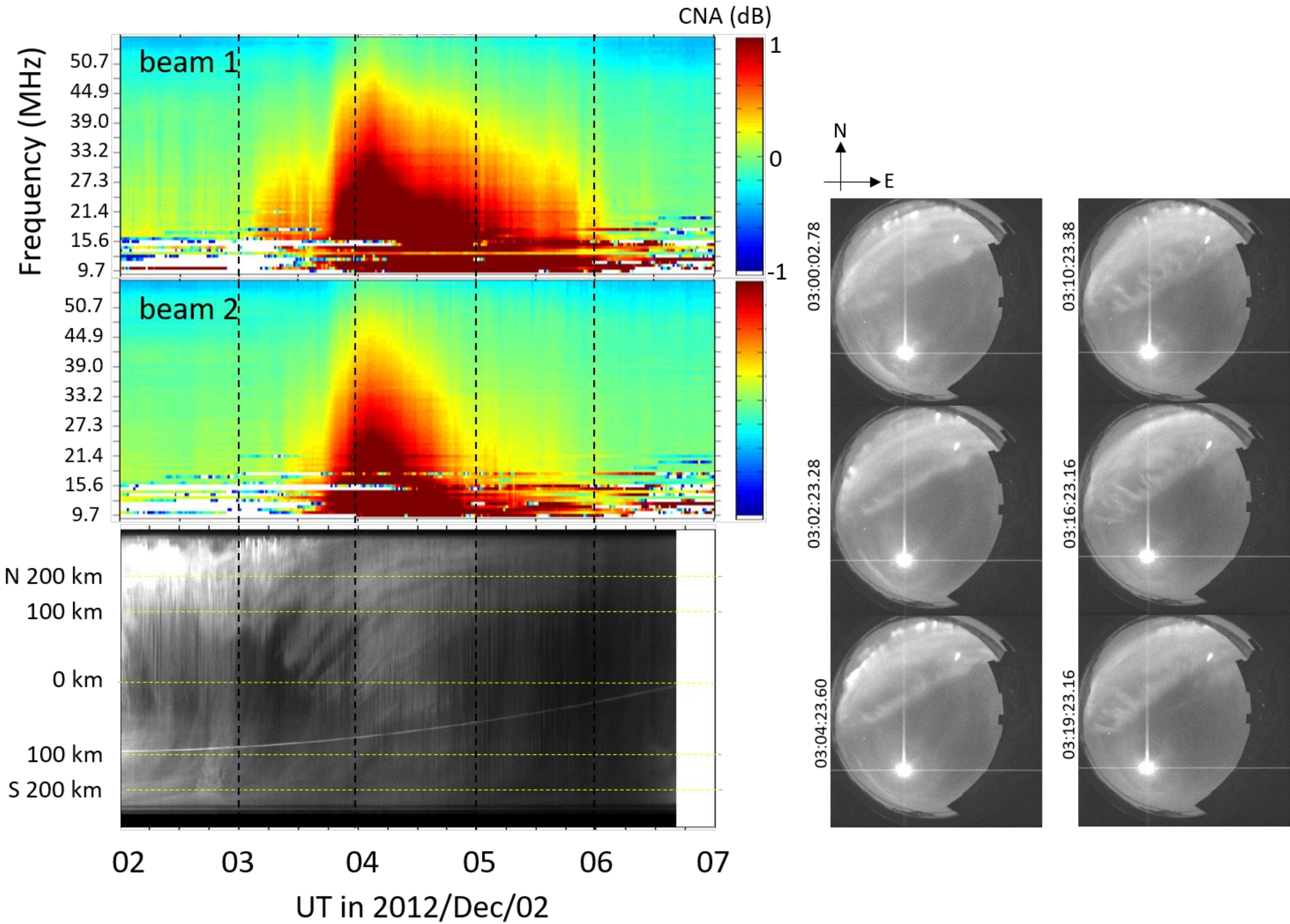

Figure 5: (Left) Figure format is the same as Figure 4 but for time interval from 02 to 07UT in 02 December 2012. Color scale for the keogram was modified to see structures more clearly. (Right) six snap-shots of the all-sky image take at Kilpisjärvi from 03:00:02 to 03:19:23 UT. A bright white spot is the lunar light.

Figure 6.

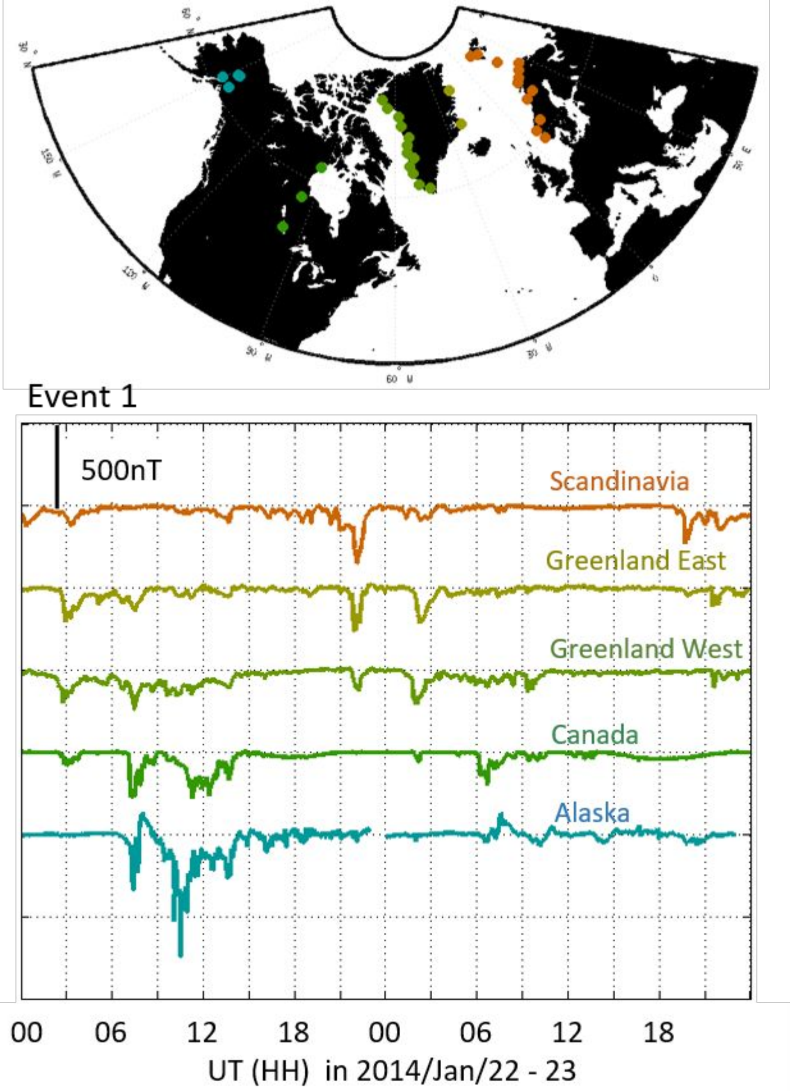

Figure 6: Top panel shows a map of the magnetometer chains employed for making local AL values, which are plotted in the bottom panel, from 00 to 20 UT in 22-23 January 2014. This presents the UT dependence of the substorm onset longitude.

Figure 7.

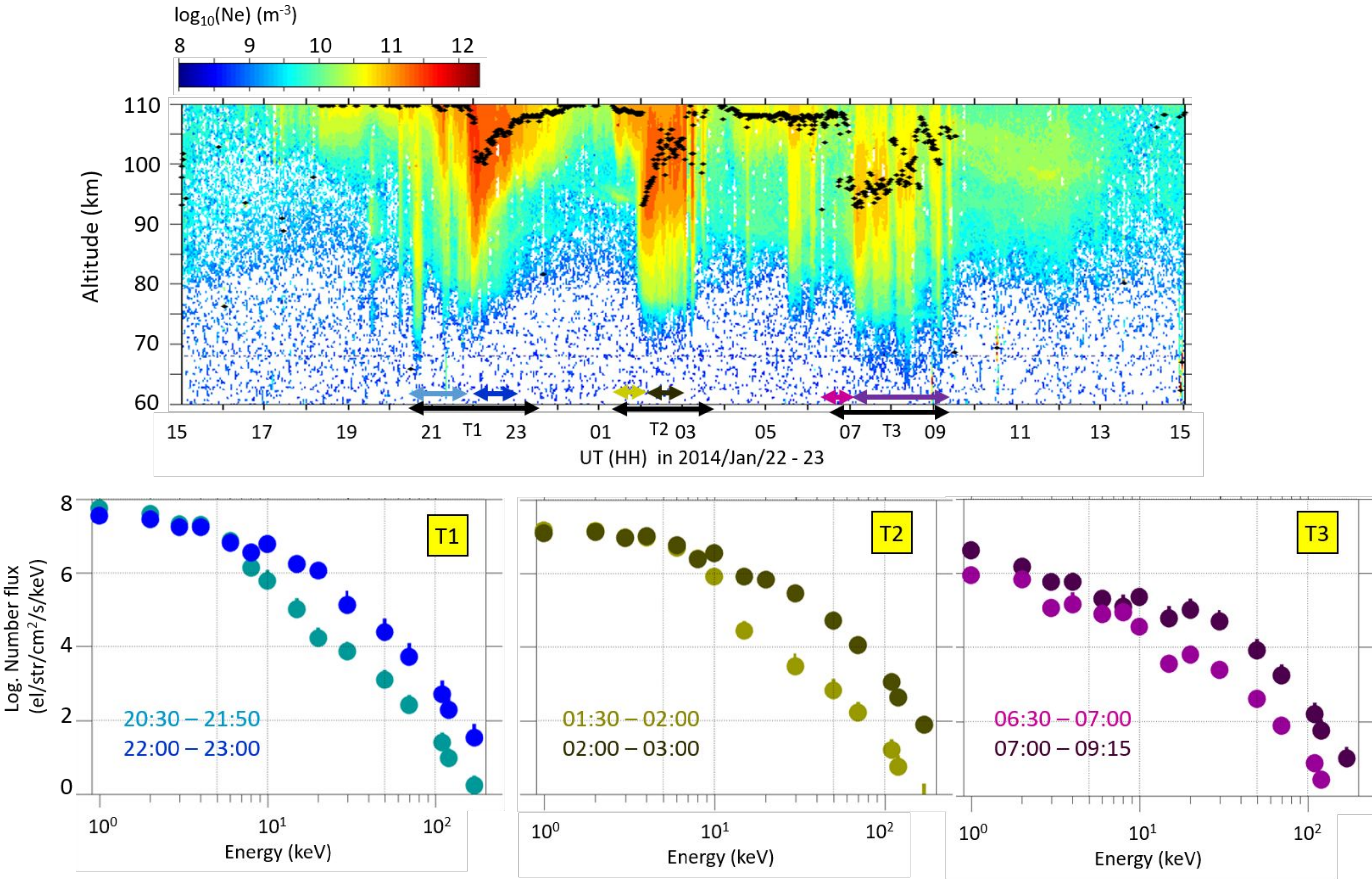

Figure 7: Electron density shown in the top panel is same as Figure 1a. The three selected time intervals, T1-3, are separated into six groups as marked by colored arrows. Bottom panels present mean energy fluxes calculated with the CARD method using the electron density at individual six time intervals. The six time intervals are written in each panel.

Figure 8.

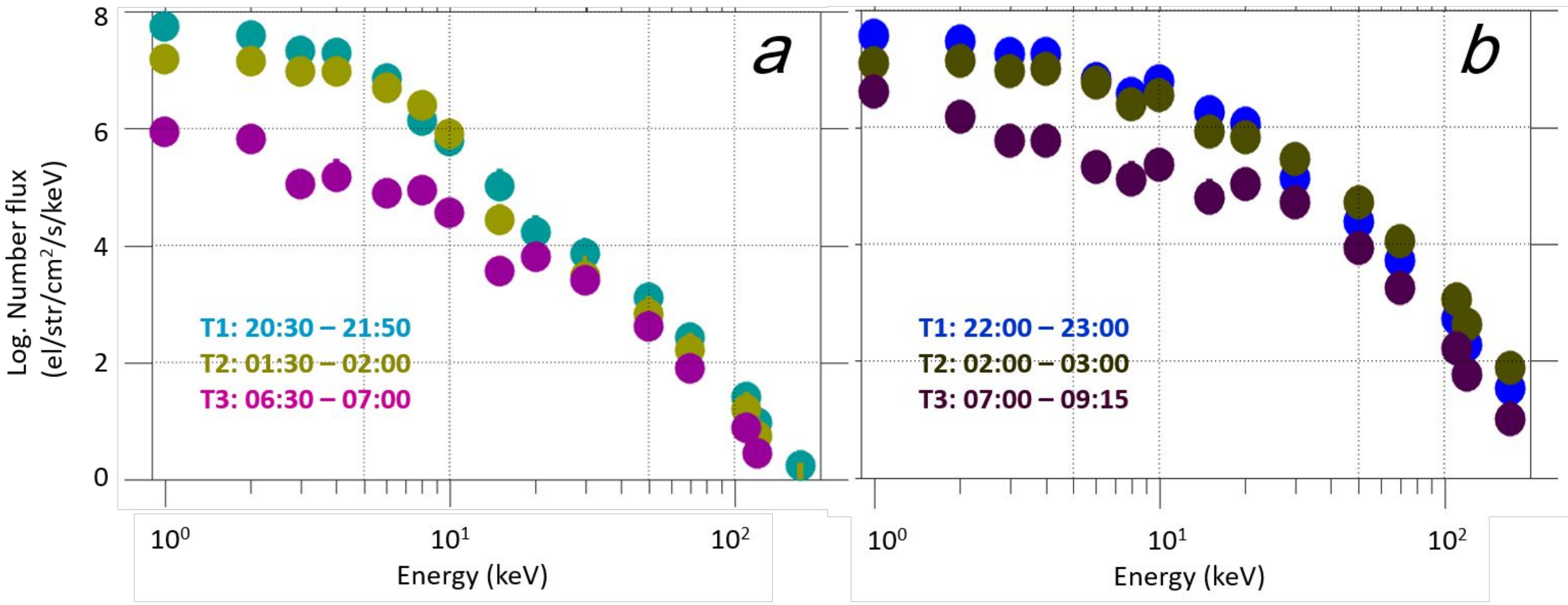

Figure 8: Same CARD spectra shown in the bottom panels of Figure 7; but separated to the time intervals of (a) relatively quieter condition and (b) more active condition.

Figure 9.

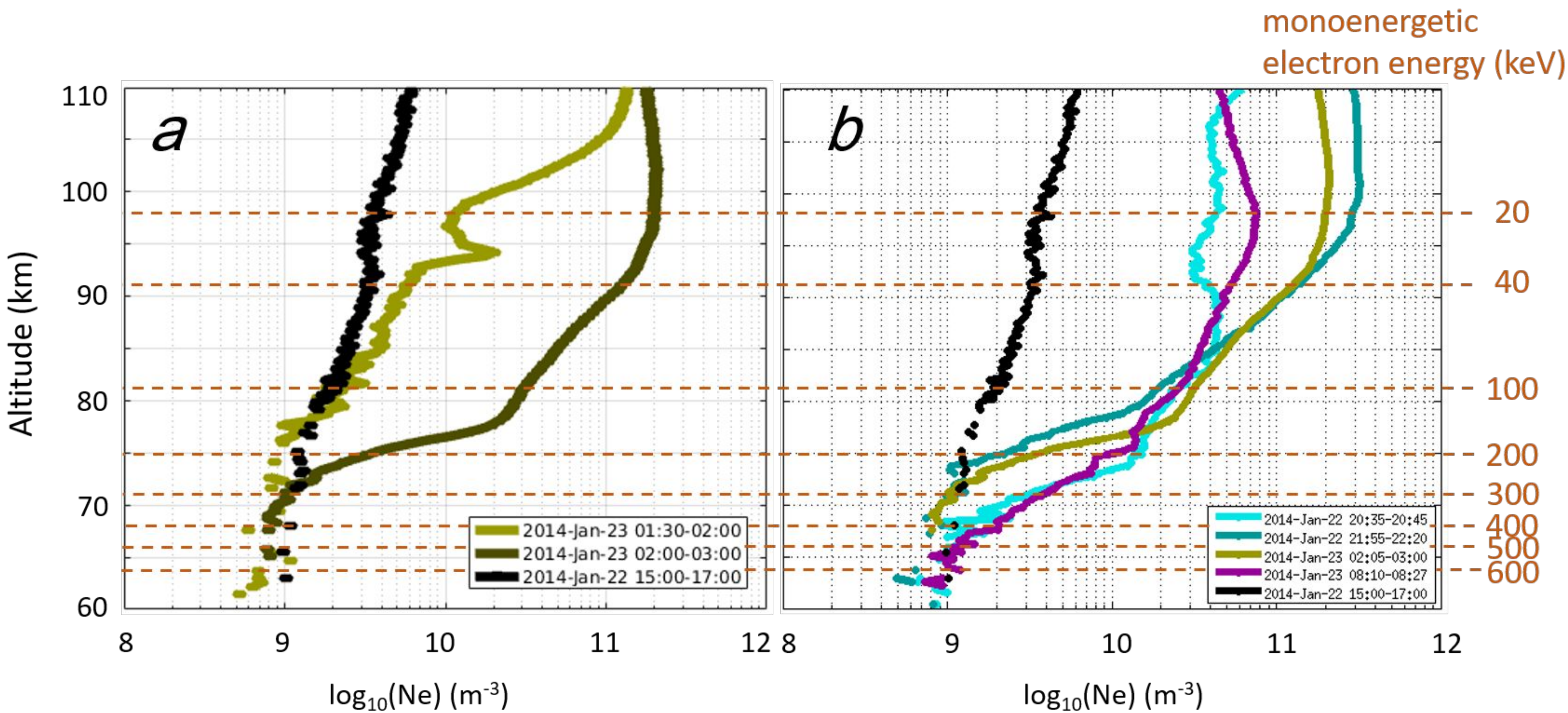

Figure 9: Mean height profiles of the electron density measured with the EISCAT VHF radar from 60 to 110 km height. Seven time intervals (written in the bottom right box) are selected to calculate the mean values. As the reference, the mean electron density during relatively quiet time period (15-17 UT in 2014 January 22) is plotted in both panels a and b (black). Two profiles in Panel a are made of measurements during T2, and four profiles in Panel b are made of measurements during the EEP events. Horizontal dashed lines are drawn at stopping heights corresponding to mono-energetic electrons at energy of numbers written at the right-hand-side of the Panel b.

Figure 10.

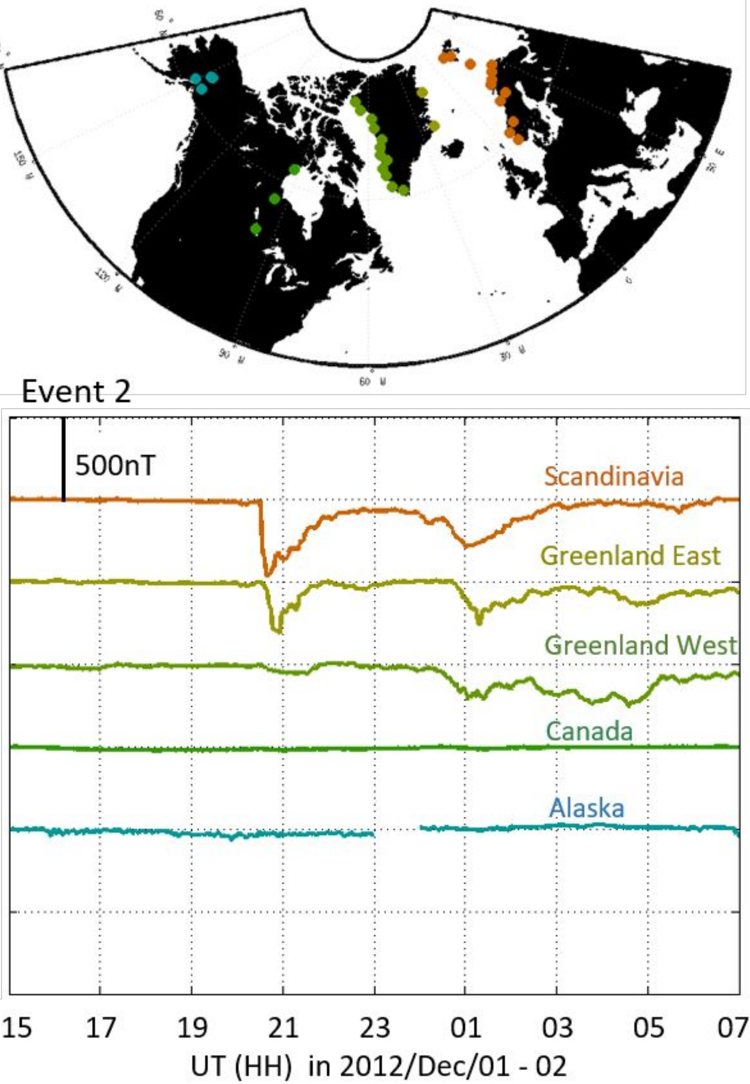

Figure 10: Figure format is same as Figure 6 but for Event 2, 01-02 December 2012.

Figure 11.

Figure 12.

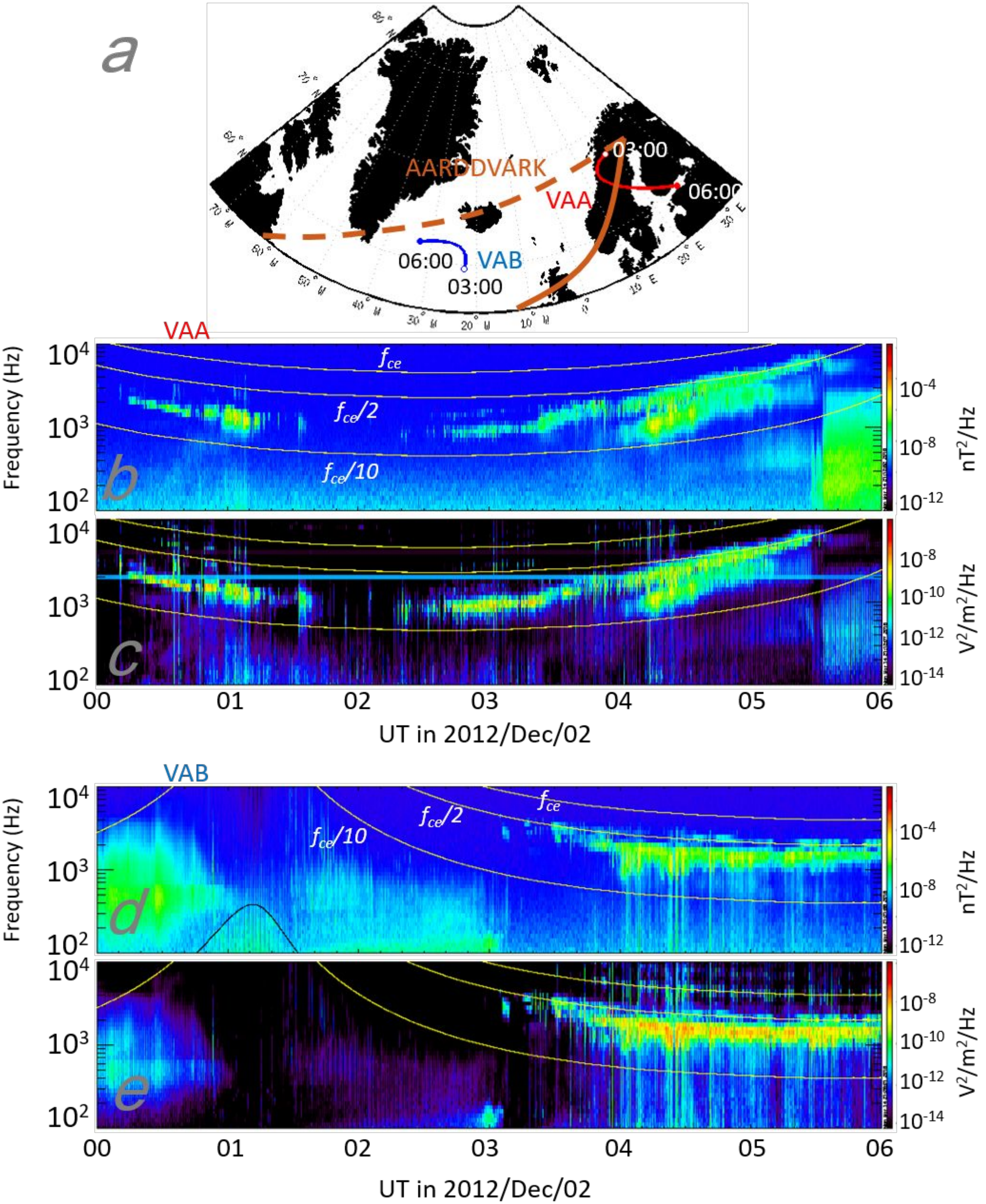

Figure 12: (a) Trajectories of Van Allen Probes A (VAA, red curve) and B (VAB, blue curve) from 03 to 06 UT in 02 December 2012. Poleward (orange dashed curve) and equatorward (orange solid curve) edge of the EEP region are drawn based on results from the AARDDVARK. (b to e) Spectra of the magnetic and electric fields, respectively, measured with the EMFISIS on VAA and VAB from 00 to 06 UT.